Radio Frequency Tunable Oscillator Device Based on a SmB_6 Microcrystal

Alex Stern,[1] Dmitry K. Efimkin,[2] Victor Galitski,[2] Zachary Fisk,[1] and Jing Xia[1]

[1]*Department of Physics and Astronomy, University of California, Irvine, California 92697, USA*
[2]*Joint Quantum Institute and Condensed Matter Theory Center, University of Maryland,
College Park, Maryland 20742-4111, USA*

Radio frequency tunable oscillators are vital electronic components for signal generation, characterization, and processing. They are often constructed with a resonant circuit and a "negative" resistor, such as a Gunn diode, involving complex structure and large footprints. Here we report that a piece of SmB_6, 100 μm in size, works as a current-controlled oscillator in the 30 MHz frequency range. SmB_6 is a strongly correlated Kondo insulator that was recently found to have a robust surface state likely to be protected by the topology of its electronics structure. We exploit its nonlinear dynamics, and demonstrate large ac voltage outputs with frequencies from 20 Hz to 30 MHz by adjusting a small dc bias current. The behaviors of these oscillators agree well with a theoretical model describing the thermal and electronic dynamics of coupled surface and bulk states. With reduced crystal size we anticipate the device to work at higher frequencies, even in the THz regime. This type of oscillator might be realized in other materials with a metallic surface and a semiconducting bulk.

Samarium Hexaboride (SmB_6) is a mixed-valence Kondo insulator [1] with many unusual properties, perhaps most well-known for its resistance-temperature dependence that resembles both a metal and an insulator [2]. Recently, SmB_6 was proposed to be a topological Kondo insulator [3,4], with a Kondo insulating gap in the bulk and a gapless (metallic) Dirac state on the surface, which is protected by time-reversal symmetry (see Ref. [5] for a recent review). This metallic surface has been verified in SmB_6 by both transport [6,7] and ARPES [8,9] experiments, with unusual spin texture [10]. The surface state survives nonmagnetic perturbations such as electric gating [11] and mechanical abrasion [6,7,11], but is destroyed by magnetic dopants that break time-reversal symmetry [12]. Quantum oscillation [13] suggests that the dispersion of the surface state is Dirac-like, similar to that of graphene. The bulk of SmB_6 is extremely insulating [6,7] and free from impurity conductions, unless under extremely high pressure [2] or magnetic field [14], when the density of states of the bulk Fermi surface starts to emerge. The combination of a truly insulating bulk, a robust surface state, and strong electronic correlation [15–18] makes SmB_6 a promising candidate to search for useful properties [5]. Up to date, most research has been focused on the equilibrium properties of SmB_6; its transient dynamics could also be interesting.

When biased with a few mA of dc current, self-heating in SmB_6 causes a large nonlinear resistance [19], which could lead to oscillation behavior. In a prior Letter [19] we found that mm-sized SmB_6 crystals coupled to an external capacitor generate ac voltages at frequencies up to kHz with a few mA of dc bias current. While we speculated that this oscillation behavior might be related to the coupled electric

and thermal dynamics of SmB_6, the exact mechanism was not understood. This was in part because the surface state had not been discovered at that time [19], making correct modeling impossible. It was unclear how and if the intricate oscillations could be pushed to higher frequencies. With the recent advancements in the understanding of SmB_6, we are now able to develop a model with both the surface and bulk states. In this model, the origin of the oscillations lies in the strong coupling between the thermal and electrical phenomena in this surface-bulk system. Sufficient Joule heating, induced by an external dc current, can heat the bulk into a less insulating state, and trigger coupled temperature and current oscillations in both bulk and surface states. This model describes various aspects of the oscillations well and predicts that the frequency will rise sharply with reduced SmB_6 surface area, which we found to be true in SmB_6 microcrystals.

Shown in Fig. 1 is a 31 MHz oscillator device based on a 100-μm-sized SmB_6 microcrystal. dc bias currents (I_0) up to 4 mA are applied through two platinum wires 25 μm in diameter that are spot-welded onto the crystal surface. And the output voltage is measured via the same platinum wires using an oscilloscope. The SmB_6 crystal itself is placed at low temperature in a cryostat, while other electronic components are held at room temperature outside the cryostat. If not explicitly stated, the measurements were performed when the cryostat is at 2 K. For mm-sized SmB_6 crystals an external capacitor is required to generate oscillation [19], such an external capacitor is found to be unnecessary for microcrystals described here, likely due to the self-capacitance [19] we found in SmB_6. The exact origin of the self-capacitance is still unclear, but it seems to
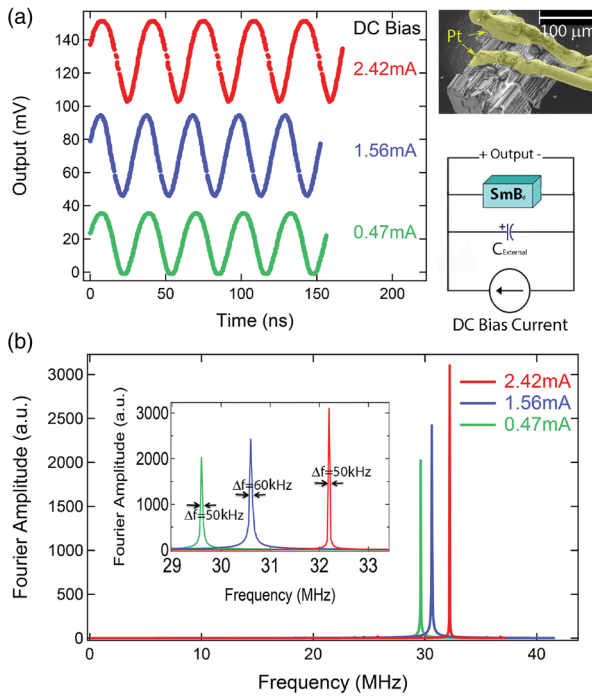
FIG. 1.   A 32 MHz SmB$_6$ oscillator. (a) Representative oscillation outputs at frequencies of 29.6, 30.6, and 32.2 MHz in ascending order, with dc bias currents of 0.47, 1.56, and 2.42 mA. Inset shows a false-color electron microscope image of the device with platinum wires colored in yellow and SmB$_6$ crystal in white. The oscillator circuit consists of dc current flowing across the crystal and a capacitor (either an external capacitor or from the self-capacitance in SmB$_6$) in parallel. An oscilloscope is then used to measure the output waveform. (b) FFT of the data in (a).

scale with the surface area, suggesting its relevance to the surface state. The oscillation behavior does not depend on the exact geometry of the crystal: as shown in the inset of Fig. 1 this oscillator is based on a rather irregularly shaped SmB$_6$ sample. The output of this oscillator can be continuously tuned from 29 to 33 MHz by varying I_0 between 0 and 4 mA. Shown in Fig. 1(a) are outputs for three representative $I_0 = 0.47$, 1.56, and 2.42 mA. And the Fourier transformations are shown in Fig. 1(b), showing a typical full width at half maximum (FWHM) spectral width Δf of only 0.05 MHz. We note that this is achieved without a phase-locked loop circuit.

We find that the center frequency, which is the frequency where maximum oscillation amplitude occurs, rises quickly with smaller SmB$_6$ crystals. Plotted in Fig. 2(a) are the center frequencies for a few representative oscillators of various sizes and geometries, versus their surface areas, which we found to show the highest correlation to center frequency, compared to volume or any single dimension. Projecting the frequency-surface area scaling further, we speculate that THz oscillations might occur for 10-μm-sized crystals. Operation above 2 THz is unlikely due to the 3.5 meV bulk activation gap in SmB$_6$. For each device, a range of external capacitors can be used to generate
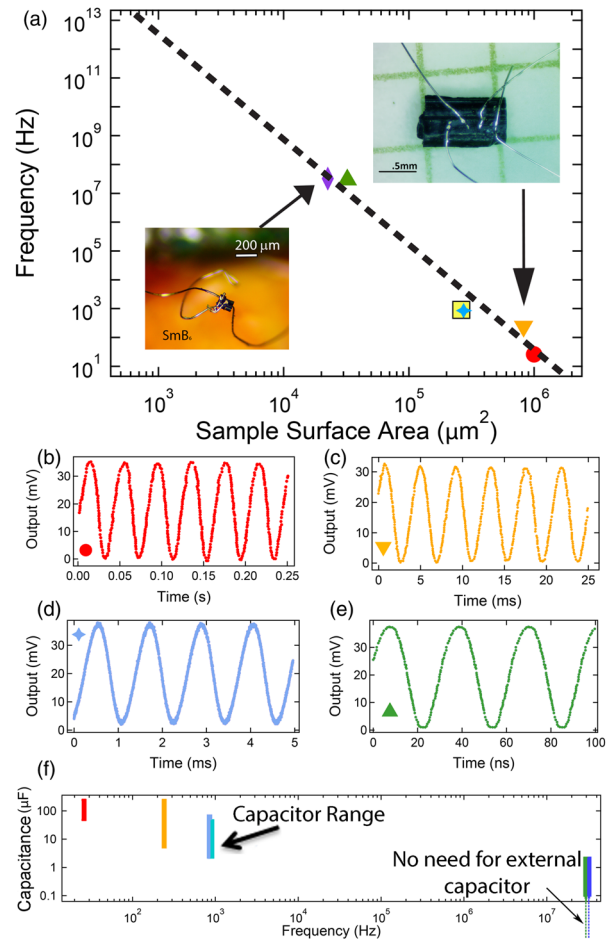

FIG. 2.   Scaling of frequency with crystal size. (a) Center frequency of oscillator devices plotted against the crystal surface area. Insets are images of 29 MHz and 250 Hz devices. The colors of the markers on this graph match the colors in (b)–(e). (b)–(e) Output waveforms of the 25 Hz, 250 Hz, 1 kHz, and 29 MHz devices, respectively. The output of the 32 MHz device is illustrated in Fig. 1. (f) The range of external capacitance values we used for each device. No external capacitors are needed for the two highest frequency (smallest) devices.

oscillations, as illustrated in Fig. 2(f) with no need for an external capacitor for the two highest frequency devices (29 and 31 MHz).

Both surface and bulk states are found to be essential for oscillation to occur. The oscillation amplitude diminishes at temperatures above 4 K, when bulk conduction dominates, or below 1 K, when surface conduction prevails. Optimal operation occurs at around 2 K when both the bulk and surface contribute to the electric conduction. This trend can be seen in the Supplemental Material [20], Fig. S2(c). It is known that in SmB$_6$, magnetic dopants such as Gd destroy the conductive surface state [12], while inducing little change to the bulk insulating gap. We fabricated several devices using crystals from the same 3% Gd doped SmB$_6$ growth batch as described in Ref. [12]. These Gd:SmB$_6$ samples are insulating to the lowest
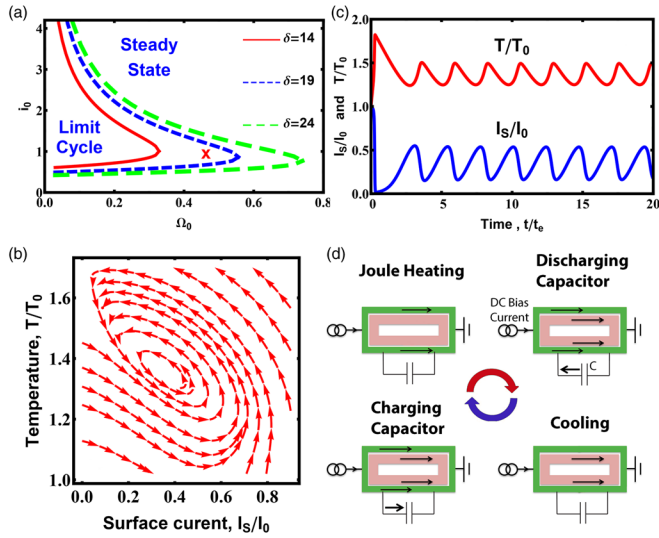
FIG. 3. Modeling the oscillation. (a) The regime diagram of the phenomenological model. The limit cycle regime supports nonlinear oscillations of temperature and currents. The red saltire symbol denotes the parameter set ($i_0 = 1.0$, $\Omega = 0.46$), for which time dependencies of the surface current and temperature, (c) and the corresponding vector flow plot (b) for the model, described by the system (1), are presented. (d) Four phases of oscillations in order, which are described in the main text: Joule heating, discharging capacitor, cooling, and charging capacitor. The arrows represent the flow of current.

measurement temperature with no sign of a conductive surface. And the measured activation gap is found to be 3.3 meV, which is very close to the 3.4–3.5 meV bulk gap in SmB_6 (see Supplemental Material [20], Fig. S4), suggesting its bulk is very similar to pure SmB_6. With the destruction of the surface state, no oscillation was observed from these crystals, despite testing a wide range of parameters such as temperature, bias current, and external capacitance. We have also performed control experiments using another well-known Kondo insulator, $Ce_3Bi_4Pt_3$ (see Supplemental Material [20], Figs. S4, S5) [21,22], which has a Kondo gap of 2.8 meV similar to that of SmB_6 but without a surface state at least down to our lowest measurement temperature of 1 K. We could not find any oscillation from $Ce_3Bi_4Pt_3$ samples.

Taking into account both surface and bulk states, we have built a model to describe the oscillations process depicted in Fig. 3(d). It is based on charge and heat conservation equations and can be casted as follows:

$$CR_S\dot{I}_S = I_0 - GI_S;$$
$$C_H\dot{T} = 2I_S^2 R_S G - I_S I_0 R_S - \gamma(T - T_0). \quad (1)$$

Here I_S and I_0 are surface and total currents through the sample; C is combined internal and external capacitance; $G = (R_S + R_B)/R_B$, where R_S and $R_B = R_B^0 \exp[-\Delta/T + \Delta/T_0]$ are the surface and bulk resistances

with insulating gap Δ; $C_H = C_H^0(T/T_0)^3$ and γ are the heat capacity dominated by phonons and heat transfer through external leads with temperature T_0. C_H^0 and R_B^0 are heat capacity and bulk resistance in the thermal equilibrium. The detailed analysis of the model is presented in Supplemental Material [20] and here we outline our main results.

In dimensionless units the dynamics of the model depend on four parameters $\rho_B = R_B^0/R_S$, $\delta = \Delta/T_0$, $\Omega = C_H^0/\gamma C R_S = t_H/t_E$, and $i_0 = \sqrt{I_0^2 R_S/\gamma T_0}$, where $t_H = C_H^0/\gamma$ and $t_E = R_S C$ are time scales of thermal and electrical processes. The latter two can be easily tuned in the experiment by the dc bias current I_0 or capacitance C, and they control the behavior of the model. For the first two we use $\delta = 18$ and $\rho_B = 80$, which correspond to a 0.7-mm-sized sample 5 (see Supplemental Material [20], Fig. S3) at $T_0 = 2$ K. The system of Eqs. (1) has only one fixed point (at which $\dot{I}_S = 0$ and $\dot{T} = 0$), which is not allowed to be a saddle one. The regime diagram of the model, presented in Fig. 3(a), has the steady state regime, corresponding to a stable fixed point. The regime is separated by the Hopf bifurcation line from the limit-cycle regime, supporting nonlinear time-dependent oscillations of the current and the temperature and corresponding to an unstable fixed point. Figures 3(b) and 3(c) present the phase curves for the system (1), which illustrates the fate of the unstable fixed point, and the result of its explicit numerical integration. The oscillations, illustrated in Fig. 3(d), can be separated into four phases. (i) Joule heating. The surface current achieves maximum, while temperature is minimum. (ii) Discharging of capacitor. The energy flows from electrical to thermal. (iii) Cooling phase. Energy dissipates to wire leads. The current is minimized, while the temperature is maximized. (iv) Charging of capacitor. The energy flows from thermal to electrical. The system is open and nonequilibrium, but during the second and fourth phases the energy of the system is approximately conserved.

In Fig. 4 we compare the modeling results with experimentally measured oscillation behavior in sample 5. The raw experimental data can be found in the Supplemental Material [20], Fig. S3. As shown in Figs. 4(a) and 4(b), oscillations appear if the capacitance is larger than the minimal value C^c and only in a finite interval of currents, $I_0^{c1} < I_0 < I_0^{c2}$, which corresponds to conditions $i_0^{c1} < i_0 < i_0^{c2}$ and $\Omega < \Omega^c$ in our model (1) according to the regime diagram in Fig. 3(a). Illustrated in Figs. 4(c) and 4(d), between I_0^{c1} and I_0^{c2} the dependence of the frequency on the current is linear, while the dependence of the amplitude has a bell-shaped dependence. For a fixed dc bias current, the amplitude of the oscillations increases with capacitance until saturation, while the frequency smoothly decreases. The critical values of currents and capacitance differ from sample
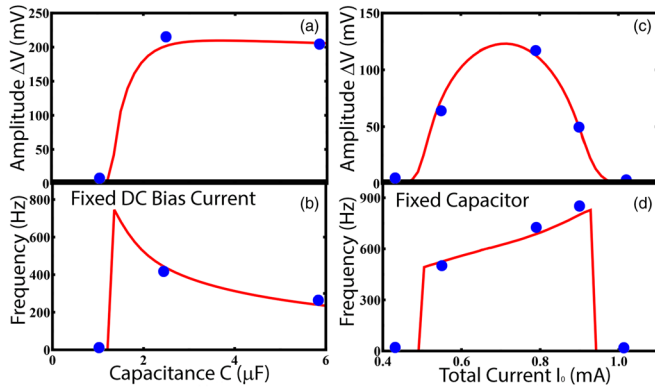
FIG. 4. Comparing the model with experimental results. Red curves are predictions from the model. Blue dots are measured valued from sample 5. The raw experimental data are shown in the Supplemental Material, Fig. S3. (a) and (b) Amplitude, ΔV and frequency ν of the voltage oscillations on capacitance C for fixed dc bias current I_0 through the sample. Blue dotted points correspond to $I_0^{exp} = 0.55$ mA, while red lines correspond to $I_0^{fit} = 0.76$ mA. (c) and (d) Amplitude ΔV and frequency ν of the voltage oscillations on dc bias current I_0, through the sample for fixed capacitance C. The blue dots correspond to $C^{exp} = 2.2$ μF, while red lines correspond $C^{fit} = 1.5$ μF.

to sample, but the behavior is general for all of them. According to our model, the oscillation frequencies are given by the inverse time scale $t_H^{-1} \approx t_E^{-1}$, which drastically decreases with sample surface area, in agreement with the experimental trend [Fig. 2(a)].

While the major focus of this Letter is on oscillators operating at low temperature based on proposed topological Kondo insulator SmB_6, the model developed here, in fact, describes a general system of a semiconductor and a metallic channel thermally and electrically coupled together. It is therefore in principle possible to realize such a tunable oscillator in other materials and at ambient temperatures. Candidate systems are Be_2Se_3/Bi_2Te_3 topological insulators [23,24], or less-exotic semiconductor quantum well heterostructures with two-dimensional electron gas. Consider a quantum well embedded in undoped narrow-band semiconductor InAs sample with length $l \sim 1$ μm, width $d \sim 1$ μm, and height $h \sim 1$ μm. At room temperatures $T \approx 300$ K undoped InAs has resistivity $\rho_B = 0.16$ Ω cm, heat capacitance $C_H^0 = 0.25$ J/g K, heat conductivity $W = 0.27$ J/(s cm K), and density $\rho_D = 5.62$ g/cm^3. As a result for a typical resistance of two-dimensional electron gas $R_S = 500$ Ω, the condition $R_S \approx R_B$ is satisfied. The parameters of our model, given by Eqs. (1), can be estimated as $\gamma = Wld/h \approx 27 \times 10^{-6}$ J/sK and $C_H = C\rho_D ldh \approx 1.3 \times 10^{-6}$ J/K. The first condition $\Omega \sim 1$ is satisfied if the time of thermal processes $t_H \approx 56$ ns matches the time of electrical processes $t_E = R_S C$, which can be achieved for a capacitance $C = 0.1$ nF. The second condition, $i_0 \sim 1$, is satisfied for electric current

$I_0 \approx \sqrt{\gamma T / R_S} \approx 4$ mA. The observation of oscillation in this nanostructure may demand fine-tuning of parameters; nevertheless, we are optimistic that the conditions can be satisfied at room temperature.

[1] G. Aeppli and Z. Fisk, Comments Condens. Matter Phys. **16**, 155 (1992).
[2] J. C. Cooley, M. C. Aronson, Z. Fisk, and P. C. Canfield, Phys. Rev. Lett. **74**, 1629 (1995).
[3] M. Dzero, K. Sun, V. Galitski, and P. Coleman, Phys. Rev. Lett. **104**, 106408 (2010).
[4] M. Dzero, K. Sun, P. Coleman, and V. Galitski, Phys. Rev. B **85**, 045130 (2012).
[5] M. Dzero, J. Xia, V. Galitski, and P. Coleman, Annu. Rev. Condens. Matter Phys. **7**, 249 (2016).
[6] D. J. Kim, S. Thomas, T. Grant, J. Botimer, Z. Fisk, and J. Xia, Sci. Rep. **3**, 3150 (2013).
[7] S. Wolgast, C. Kurdak, K. Sun, J. W. Allen, D. J. Kim, and Z. Fisk, Phys. Rev. B **88**, 180405 (2013).
[8] M. Neupane, N. Alidoust, S. Y. Xu, T. Kondo, Y. Ishida, D. J. Kim, C. Liu, I. Belopolski, Y. J. Jo, T. R. Chang, H. T. Jeng, T. Durakiewicz, L. Balicas, H. Lin, A. Bansil, S. Shin, Z. Fisk, and M. Z. Hasan, Nat. Commun. **4**, 2991 (2013).
[9] N. Xu, X. Shi, P. K. Biswas, C. E. Matt, R. S. Dhaka, Y. Huang, N. C. Plumb, M. Radović, J. H. Dil, E. Pomjakushina, K. Conder, A. Amato, Z. Salman, D. M. Paul, J. Mesot, H. Ding, and M. Shi, Phys. Rev. B **88**, 121102 (2013).
[10] N. Xu *et al.*, Nat. Commun. **5**, 4566 (2014).
[11] P. Syers, D. Kim, M. S. Fuhrer, and J. Paglione, Phys. Rev. Lett. **114**, 096601 (2015).
[12] D. J. Kim, J. Xia, and Z. Fisk, Nat. Mater. **13**, 466 (2014).
[13] G. Li, Z. Xiang, F. Yu, T. Asaba, B. Lawson, P. Cai, C. Tinsman, A. Berkley, S. Wolgast, Y. S. Eo, D.-J. Kim, C. Kurdak, J. W. Allen, K. Sun, X. H. Chen, Y. Y. Wang, Z. Fisk, and L. Li, Science **346**, 1208 (2014).
[14] B. S. Tan, Y.-T. Hsu, B. Zeng, M. C. Hatnean, N. Harrison, Z. Zhu, M. Hartstein, M. Kiourlappou, A. Srivastava, M. D. Johannes, T. P. Murphy, J.-H. Park, L. Balicas, G. G. Lonzarich, G. Balakrishnan, and S. E. Sebastian, Science **349**, 287 (2015).
[15] V. Alexandrov, P. Coleman, and O. Erten, Phys. Rev. Lett. **114**, 177202 (2015).
[16] D. K. Efimkin and V. Galitski, Phys. Rev. B **90**, 081113 (2014).
[17] J. Iaconis and L. Balents, Phys. Rev. B **91**, 245127 (2015).
[18] P. Nikolić, Phys. Rev. B **90**, 235107 (2014).
[19] D. J. Kim, T. Grant, and Z. Fisk, Phys. Rev. Lett. **109**, 096601 (2012).
[20] See Supplemental Material at http://link.aps.org/supplemental/10.1103/PhysRevLett.116.166603 for device

fabrication, detailed analysis of the model, additional raw data plots, and control samples.

[21] M. F. Hundley, P. C. Canfield, J. D. Thompson, Z. Fisk, and J. M. Lawrence, Phys. Rev. B **42**, 6842 (1990).

[22] J. C. Cooley, M. C. Aronson, and P. C. Canfield, Phys. Rev. B **55**, 7533 (1997).

[23] X.-L. Qi and S.-C. Zhang, Rev. Mod. Phys. **83**, 1057 (2011).

[24] M. Z. Hasan and C. L. Kane, Rev. Mod. Phys. **82**, 3045 (2010).